Atomic Layer Etching of Al_2O_3 Using Sequential, Self-Limiting Thermal Reactions with $Sn(acac)_2$ and Hydrogen Fluoride

Younghee Lee[†] and Steven M. George[*,†,‡]

[†]Department of Chemistry and Biochemistry, [‡]Department of Mechanical Engineering, University of Colorado, Boulder, Colorado 80309, United States

ABSTRACT

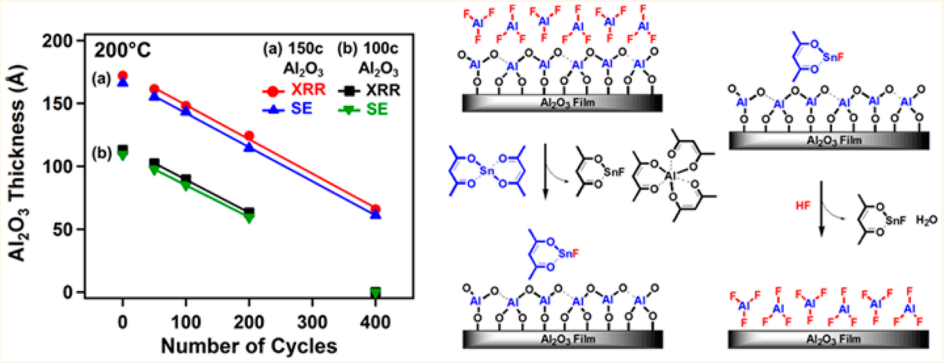

The atomic layer etching (ALE) of Al_2O_3 was demonstrated using sequential, self-limiting thermal reactions with tin(II) acetylacetonate ($Sn(acac)_2$) and hydrogen fluoride (HF) as the reactants. The Al_2O_3 samples were Al_2O_3 atomic layer deposition (ALD) films grown using trimethylaluminum and H_2O. The HF source was HF-pyridine. Al_2O_3 was etched linearly with atomic level precision *versus* number of reactant cycles. The Al_2O_3 ALE was monitored at temperatures from 150 to 250 °C. Quartz crystal microbalance (QCM) studies revealed that the sequential $Sn(acac)_2$ and HF reactions were self-limiting *versus* reactant exposure. QCM measurements also determined that the mass change per cycle (MCPC) increased with temperature from −4.1 ng/(cm^2 cycle) at 150 °C to −18.3 ng/(cm^2 cycle) at 250 °C. These MCPC values correspond to etch rates from 0.14 Å/cycle at 150 °C to 0.61 Å/cycle at 250 °C based on the Al_2O_3 ALD film density of 3.0 g/cm^3. X-ray reflectivity (XRR) analysis confirmed the linear removal of Al_2O_3 and measured an Al_2O_3 ALE etch rate of 0.27 Å/cycle at 200 °C. The XRR measurements also indicated that the Al_2O_3 films were smoothed by Al_2O_3 ALE. The overall etching reaction is believed to follow the reaction $Al_2O_3 + 6Sn(acac)_2 + 6HF \rightarrow 2Al(acac)_3 + 6SnF(acac) + 3H_2O$. In the proposed reaction mechanism, the $Sn(acac)_2$ reactant donates acac to the substrate to produce $Al(acac)_3$. The HF reactant allows SnF(acac) and H_2O to leave as reaction products. The thermal ALE of many other metal oxides using $Sn(acac)_2$ or other metal β-diketonates, together with HF, should be possible by a similar mechanism. This thermal ALE mechanism may also be applicable to other materials such as metal nitrides, metal phosphides, metal sulfides and metal arsenides.

KEYWORDS: atomic layer etching · Al_2O_3 · sequential exposures · thermal reactions · quartz crystal microbalance · X-ray reflectivity · atomic layer deposition

Atomic layer deposition (ALD) is a thin film growth technique based on sequential, self-limiting surface reactions.[1] ALD can deposit extremely conformal thin films with atomic layer control. ALD has developed rapidly over the last 10−15 years to meet many industrial needs such as the miniaturization of semiconductor devices.[1] ALD can deposit a wide range of materials from metal oxides to metals.[2] ALD is typically accomplished using thermal chemistry. However, sometimes plasma ALD is employed to enhance the surface reactions.[3]

In contrast, atomic layer etching (ALE) is a thin film removal technique based on sequential, self-limiting surface reactions.[4−6] ALE can be viewed as the reverse of ALD. ALE should be able to remove thin films conformally and isotropically with atomic

* Address correspondence to steven.george@colorado.edu.

Received for review December 19, 2014 and accepted January 20, 2015.

Published online January 20, 2015
10.1021/nn507277f

layer control. Compared with the large number of ALD processes,[2] ALE processes have not been defined for as many materials. In addition, no thermal chemical processes have been reported for ALE. The ALE processes that have been reported have used excitation such as ion-enhanced or energetic noble gas atom-enhanced surface reactions.[4−6] Most of the reported ALE processes have adsorbed a halogen on the surface of the material. Ion or noble gas atom bombardment is then used to desorb halogen compounds that etch the material.[4−6]

Most of the reports of ALE have focused on the ALE of Si, Ge, compound semiconductors, oxides and carbon substrates. Si ALE has been accomplished using either Cl or F adsorption that is subsequently followed by the removal of silicon halides using Ar^+ ion bombardment.[5−10] Very similar approaches are employed for Ge ALE.[11,12] Alternative approaches for Si ALE utilize energetic neutral Ar beam bombardment.[13] GaAs ALE has been demonstrated using Cl adsorption followed by excitation with either Ar^+ ions,[14] 100 eV electrons,[15] or UV radiation.[16,17] InP ALE has also been accomplished using Cl adsorption and energetic neutral Ne beam bombardment.[18]

The ALE of a variety of oxides have been reported based on the adsorption of Cl using BCl_3 and the removal of chloride compounds using an energetic Ar atom neutral beam. This approach has been used for the ALE of Al_2O_3,[19] HfO_2,[20] ZrO_2,[21] and TiO_2.[22] SiO_2 ALE has also been performed using fluorocarbon adsorption followed by Ar^+ ion bombardment.[23,24] The ALE of various carbon substrates have also been accomplished using oxygen radical adsorption followed by material removal using Ar^+ ion bombardment or an energetic Ar neutral beam. This approach has been demonstrated for graphite,[25] graphene[26] and polymer material.[27]

Developing thermal self-limiting ALE reactions that are the reverse of ALD reactions will be difficult. Thermal ALD reactions are typically exothermic and extremely favorable thermochemical reactions.[1] These thermal reactions are spontaneous with negative ΔG values where G is the Gibbs free energy. Performing ALD reactions in reverse will not occur because of these thermodynamic considerations. The challenge for thermal ALE reactions is to find alternative, self-limiting reactions with different reactants that are exothermic and display negative ΔG values to ensure a spontaneous reaction.

In this paper, sequential exposures of tin(II) acetylacetonate ($Sn(acac)_2$) and hydrogen fluoride (HF) are employed for the thermal ALE of Al_2O_3. The thermal Al_2O_3 ALE reactions are examined using quartz crystal microbalance (QCM) studies. The Al_2O_3 film thicknesses are measured using X-ray reflectivity (XRR) analysis. The QCM and XRR measurements can determine if the Al_2O_3 etching is linear *versus* the number of $Sn(acac)_2$ and HF reaction cycles. The QCM measurements can evaluate whether the Al_2O_3 ALE is self-limiting *versus* the $Sn(acac)_2$ and HF exposure times. This new method for ALE based on sequential, self-limiting, thermal reactions with $Sn(acac)_2$ and HF as the reactants broadens the strategies for ALE reactions.

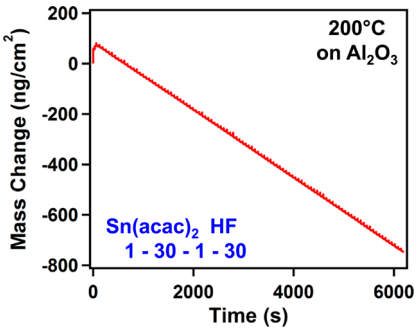

Figure 1. Mass change *versus* time for Al_2O_3 ALE using sequential $Sn(acac)_2$ and HF exposures at 200 °C.

RESULTS AND DISCUSSION

Quartz Crystal Microbalance Studies. Figure 1 shows the mass change during 100 ALE cycles of $Sn(acac)_2$ and HF reactions on an Al_2O_3 surface at 200 °C. The initial Al_2O_3 ALD film on the QCM surface was prepared by 100 cycles of Al_2O_3 ALD using TMA and H_2O at 200 °C. One ALE cycle consisted of a $Sn(acac)_2$ dose of 1 s, an N_2 purge of 30 s, a HF dose of 1 s, and a second N_2 purge of 30 s. This reaction sequence is denoted as 1−30−1−30. Pressure transients during $Sn(acac)_2$ and HF doses were 20 and 80 mTorr, respectively.

The etching of the Al_2O_3 film in Figure 1 is very linear and displays a mass change per cycle (MCPC) = −8.4 ng/(cm^2 cycle). This MCPC corresponds to an etch rate of 0.28 Å/cycle based on the Al_2O_3 ALD film density of 3.0 g/cm^3 measured by XRR. All ALE cycles show mass loss resulting from the etching of the Al_2O_3 film except during the first ALE cycle. The first cycle displays mass gains of ΔM_{Sn} = 57 ng/cm^2 and ΔM_{HF} = 13 ng/cm^2.

The mass gain for ΔM_{Sn} on the first cycle is attributed to $Sn(acac)_2$ adsorption on the hydroxylated Al_2O_3 surface. $Sn(acac)_2$ could adsorb either molecularly as $Sn(acac)_2$* or dissociatively as Sn(acac)* and (acac)* where the asterisks designate a surface species. This adsorption would lead to a mass increase. In addition, the mass gain for ΔM_{HF} on the first cycle is attributed to the formation of AlF_3 by the reaction of HF with the underlying Al_2O_3 surface. The reaction $Al_2O_3 + 6HF \rightarrow 2AlF_3 + 3H_2O$ is spontaneous with ΔG = −58 kcal at 200 °C.[28] AlF_3 formation has also been confirmed by *in situ* Fourier transform infrared (FTIR) spectroscopy studies that will be presented in another publication.[29] The first cycle of $Sn(acac)_2$ and HF exposures establishes the initial $Sn(acac)_2$ and AlF_3 species on the Al_2O_3 substrate.

Figure 2 shows an enlargement of the mass losses *versus* time at 200 °C for three cycles in the steady state

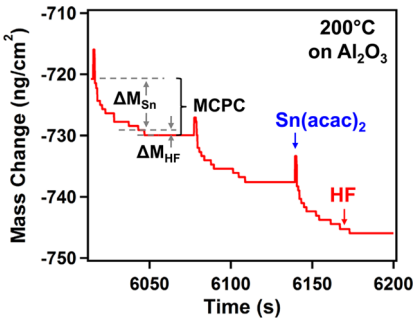

Figure 2. Expansion of linear region of Figure 1 showing the individual mass changes during the sequential $Sn(acac)_2$ and HF exposures at 200 °C.

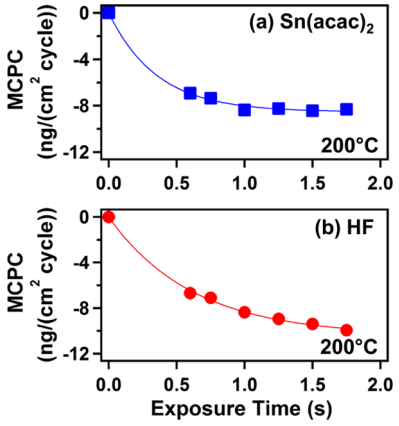

Figure 3. Mass change per cycle (MCPC) *versus* precursor exposure time at 200 °C for (a) $Sn(acac)_2$ and (b) HF.

linear etching regime in Figure 1. There is a gradual mass decrease after a short mass gain coinciding with the $Sn(acac)_2$ exposure. This behavior suggests $Sn(acac)_2$ adsorption followed by either $Sn(acac)_2$ desorption and/or the removal of reaction products. A mass loss of $\Delta M_{Sn} = -8.1$ ng/cm^2 was observed after 1 s of $Sn(acac)_2$ exposure. In contrast, the HF exposure leads to little mass loss. A mass loss of $\Delta M_{HF} = -0.28$ ng/cm^2 was observed after 1 s of HF exposure.

Figure 3 examines the self-limiting nature of the Al_2O_3 ALE reactions at 200 °C. These MCPCs were measured *versus* different reactant exposure times. Figure 3a shows the self-limiting behavior of the $Sn(acac)_2$ reaction using different $Sn(acac)_2$ exposure times with a single 1 s exposure of HF. A constant N_2 purge of 30 s was used after each exposure. This reaction sequence can be denoted as $x-30-1-30$. The MCPC *versus* $Sn(acac)_2$ exposure time decreases quickly and levels off at MCPC = −8 ng/(cm^2 cycle).

Figure 3b examines the self-limiting behavior of the HF reaction using different HF exposure times with a single 1 s exposure of $Sn(acac)_2$. This reaction sequence can be denoted as $1-30-x-30$. The MCPC *versus* HF exposure time deceases and then levels off. The slow change in the MCPC beyond −8 ng/(cm^2 cycle) for longer HF exposures >1 s is believed to be caused by larger HF background pressures and longer HF residence

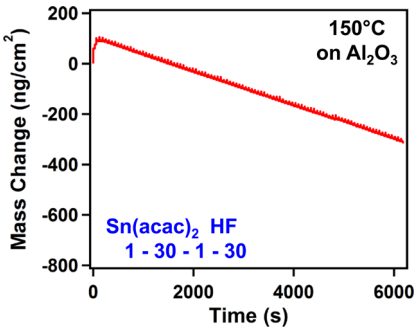

Figure 4. Mass change *versus* time for Al_2O_3 ALE using sequential $Sn(acac)_2$ and HF exposures at 150 °C.

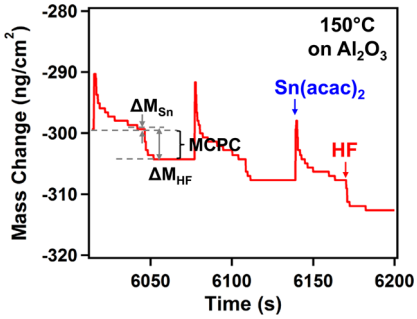

Figure 5. Expansion of linear region of Figure 4 showing the individual mass changes during the sequential $Sn(acac)_2$ and HF exposures at 150 °C.

times that lead to some chemical vapor etching (CVE) during the $Sn(acac)_2$ exposures. Figure 3a and 3b together show that the $Sn(acac)_2$ and HF reactions display nearly self-limiting behavior. The MCPC = −8 ng/(cm^2 cycle) for 1 s exposures of $Sn(acac)_2$ and HF was independent of purge time for purge times between 20 and 120 s.

Figure 4 shows the mass change during 100 ALE cycles of $Sn(acac)_2$ and HF reactions on an Al_2O_3 surface at 150 °C using a reaction sequence of $1-30-1-30$. The initial Al_2O_3 film was prepared by 100 cycles of Al_2O_3 ALD using TMA and H_2O at 150 °C. The etching of the Al_2O_3 film is very linear with MCPC = −4.1 ng/(cm^2 cycle). This MCPC corresponds to an etch rate of 0.14 Å/cycle based on the Al_2O_3 ALD film density of 3.0 g/cm^3 measured by XRR.

Figure 5 shows an enlargement of the mass losses *versus* time at 150 °C for three cycles in the steady state linear etching regime in Figure 4. There are distinct differences between the mass changes during the etching reactions at 200 and 150 °C. A mass gain of $\Delta M_{Sn} = +0.19$ ng/cm^2 was observed after the $Sn(acac)_2$ exposure for 1 s at 150 °C. In contrast, a mass loss of $\Delta M_{Sn} = -8.1$ ng/cm^2 was obtained at 200 °C. This difference may be attributed to more stable $Sn(acac)_2$ reaction products on the surface at 150 °C.

A mass decrease of $\Delta M_{HF} = -4.3$ ng/cm^2 was observed after the HF exposure for 1 s at 150 °C. This mass decrease is much larger than the mass decrease of $\Delta M_{HF} = -0.28$ ng/cm^2 at 200 °C. However, if more

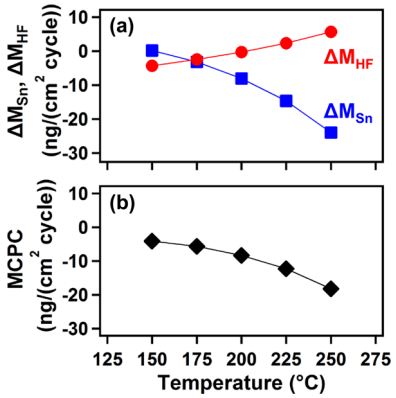

Figure 6. Temperature dependence of (a) ΔM_{Sn} and ΔM_{HF} and (b) MCPC for Al_2O_3 ALE.

$Sn(acac)_2$ reaction products remain on the surface following the $Sn(acac)_2$ exposure at 150 °C, then more $Sn(acac)_2$ reaction products can be lost during the HF reaction. This behavior would explain the mass gain after the $Sn(acac)_2$ exposure and larger mass loss after the HF exposure at 150 °C.

The ΔM_{Sn}, ΔM_{HF}, and MCPC values at all the reaction temperatures are shown in Figure 6. All ALE reactions were performed using a reaction sequence of 1−30−1−30 on initial Al_2O_3 surfaces. Figure 6a displays the ΔM_{Sn} and ΔM_{HF} values obtained at different reaction temperatures. ΔM_{Sn} displays a slight mass gain at 150 °C and progressively larger mass losses at higher temperatures. In contrast, ΔM_{HF} displays a mass loss at temperatures between 150 and 200 °C and mass gains at higher temperatures.

Figure 6b shows the MCPC where MCPC = ΔM_{Sn} + ΔM_{HF}. All the temperatures display a mass loss and the mass loss is larger at higher temperatures. The MCPC in Figure 6b correlates well with ΔM_{Sn} in Figure 6a. This correspondence shows that the mass change during the $Sn(acac)_2$ reaction is primarily responsible for the temperature dependence of the mass loss during Al_2O_3 ALE. ΔM_{Sn}, ΔM_{HF}, and MCPC at the different reaction temperatures are summarized in Table 1.

X-ray Reflectivity Studies. Al_2O_3 ALE was also examined using *ex situ* XRR studies. For these experiments, Al_2O_3 ALD films with a thickness of 172 Å were grown on Si(100) wafers at 200 °C. These Al_2O_3 ALD films were deposited using 150 cycles of TMA and H_2O with a reaction sequence of 1−20−1−20. Figure 7 displays XRR scans of the Al_2O_3 ALD films on the Si wafers *versus* number of $Sn(acac)_2$ and HF reaction cycles at 200 °C. The XRR scans have been displaced from each other for clarity in presentation. These XRR scans are consistent with very uniform and smooth Al_2O_3 films.

Figure 7a shows the XRR scan of the initial Al_2O_3 ALD film grown on Si(100). The Al_2O_3 ALD film thickness of 172 Å can be obtained by fitting the reflected X-ray intensity *versus* incident angle. Figure 7b, 7c, 7d, and 7e show XRR scans of the etched Al_2O_3 film after

TABLE 1. ΔM_{Sn}, ΔM_{HF} and MCPC for Al_2O_3 ALE at Different Temperatures

temperature (°C)	ΔM_{Sn} ng/(cm² cycle)	ΔM_{HF} ng/(cm² cycle)	MCPC ng/(cm² cycle)
150	0.19	−4.3	−4.1
175	−3.2	−2.4	−5.6
200	−8.1	−0.28	−8.4
225	−14.6	2.3	−12.3
250	−24.0	5.7	−18.3

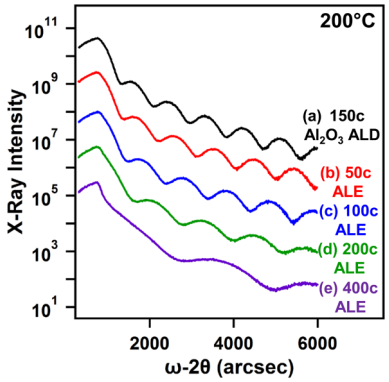

Figure 7. X-ray reflectivity scans showing X-ray intensity *versus* incident angle for Al_2O_3 films on Si(100). (a) Initial Al_2O_3 film grown using 150 Al_2O_3 ALD cycles; and Al_2O_3 films after various numbers of Al_2O_3 ALE cycles: (b) 50, (c) 100, (d) 200 and (e) 400 cycles.

50, 100, 200, and 400 ALE cycles at 200 °C, respectively. The Al_2O_3 thicknesses decrease with increasing number of ALE cycles. This decreasing film thickness is revealed by the longer modulation periods for the X-ray intensity *versus* angle after higher numbers of ALE cycles. The position of the critical angle of all the etched Al_2O_3 films is also constant. This constant critical angle indicates that there is no change of the film density during the ALE reactions.

The etched Al_2O_3 films are very smooth and do not roughen *versus* Al_2O_3 ALE. The XRR measurements yielded a roughness of the initial Al_2O_3 ALD film of ~5 Å. The surface roughness obtained by XRR analysis then decreased to ~2−3 Å after 50, 100, 200, and 400 ALE cycles at 200 °C. The XRR measurements suggest that the ALE process is able to smooth the surface of the initial Al_2O_3 films. The error in these XRR surface roughness measurements is ~1 Å. Atomic force microscope (AFM) measurements also examined the Al_2O_3 film after Al_2O_3 ALE at 200 °C. The AFM root-mean squared (RMS) surface roughness was 2.5 Å, 2.8 and 2.6 Å for the bare Si(100) wafer, an Al_2O_3 ALD film on Si(100) grown using 150 Al_2O_3 ALD cycles and the same Al_2O_3 film etched using 400 Al_2O_3 ALE cycles, respectively. This AFM analysis indicates that the Al_2O_3 film remained smooth during Al_2O_3 ALE.

Figure 8 shows the XRR measurements of the initial Al_2O_3 film thickness and the Al_2O_3 film thickness after 50, 100, 200, and 400 ALE cycles at 200 °C. For the Al_2O_3 films with an initial thickness of 172 Å in Figure 8a, the

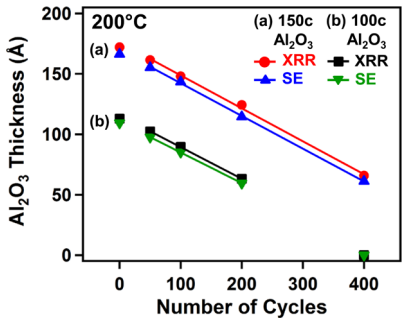

Figure 8. X-ray reflectivity and spectroscopic ellipsometry measurements of Al_2O_3 film thickness *versus* number of Al_2O_3 ALE cycles for initial Al_2O_3 ALD films grown using (a) 150 Al_2O_3 ALD cycles and (b) 100 Al_2O_3 ALD cycles.

film thickness *versus* number of ALE cycles is very linear and yields an etch rate of 0.27 Å/cycle. The spectroscopic ellipsometry (SE) measurements on these same samples yield an etch rate of 0.27 Å/cycle with an initial Al_2O_3 ALD film thickness of 166 Å. The initial thickness of the Al_2O_3 film is not used to obtain the etch rate because of the mass gain that occurs on the first ALE cycle.

The y-intercepts for the linear least-squares fitting in Figure 8a are 176 and 169 Å by XRR and SE, respectively. These thicknesses are slightly higher than initial thicknesses of 172 and 166 Å measured by XRR and SE, respectively. These larger thicknesses originate from the mass gain that occurs during nucleation of the ALE process on the first ALE cycle. The SE analysis also determined a refractive index of $n = 1.70$ for the Al_2O_3 film at a wavelength of 589 nm. This refractive index for the Al_2O_3 film remained at $n = 1.69-1.70$ after 50, 100, and 200 ALE cycles.

XRR measurements were also performed on Al_2O_3 ALD films with a thickness of 113 Å that were grown on Si(100) wafers. These Al_2O_3 ALD films were deposited at 200 °C using 100 cycles of TMA and H_2O with a reaction sequence of 1−20−1−20. Figure 8b displays the film thickness *versus* number of $Sn(acac)_2$ and HF reaction cycles at 200 °C. The XRR measurements yield an Al_2O_3 ALE etch rate of 0.26 Å/cycle. The SE measurements also yield an etch rate of 0.25 Å/cycle with an initial Al_2O_3 ALD film thickness of 109 Å. The initial thickness of the Al_2O_3 film is again not employed to determine the etch rate because of the mass gain that occurs on the first ALE cycle.

The *y*-intercepts for the linear least-squares fitting in Figure 8b are 116 and 110 Å by XRR and SE, respectively. These thicknesses are again slightly higher than the initial thicknesses of 113 and 109 Å measured by XRR and SE, respectively. These larger thicknesses originate from the mass gain that occurs on the first ALE cycle. After 400 ALE cycles for this thinner Al_2O_3 film, the XRR and SE measurements in Figure 8b indicate that the Al_2O_3 film is completely removed from the Si(100) wafer.

X-ray photoelectron spectroscopy (XPS) measurements were employed to determine the elements on the Al_2O_3 film after Al_2O_3 ALE. The XPS analysis measured Sn $3d_{5/2}$ XPS signals of 1 at. % and F 1s XPS signals of 6 at. % after 200 or 400 Al_2O_3 ALE cycles after the HF exposure. These XPS signals are consistent with AlF_3 formation and residual $Sn(acac)_2$ adsorption products. The Sn and F XPS signals were removed completely below the XPS detection limit after Ar ion sputtering for 2 min. This sputtering time is the time required to remove adventitious carbon from the surface.

Proposed ALE Reaction Mechanism. Figure 9 shows the schematic for the proposed ALE reaction mechanism. This mechanism is based on the mass changes during the $Sn(acac)_2$ and HF exposures as determined by the QCM measurements.

During the $Sn(acac)_2$ reaction (A), the $Sn(acac)_2$ reacts with the AlF_3 layer on the Al_2O_3 substrate. This AlF_3 layer is formed from the reaction of Al_2O_3 with HF after several ALE reactions on the initial Al_2O_3 surface. The $Sn(acac)_2$ reacts with the AlF_3 layer to form volatile SnF(acac) and $Al(acac)_3$ reaction products and SnF(acac)* surface species. The slow loss of mass in Figures 2 and 5 after the $Sn(acac)_2$ exposure is attributed to the slow desorption of acac species.[30,31] SnF_2 formation is unlikely because $Sn(acac)_2$ is expected to react with AlF_3 to form volatile SnF(acac) and $Al(acac)_3$ until depleting the AlF_3 layer. After the AlF_3 layer is lost resulting from $Al(acac)_3$ and SnF(acac) product formation, there may be a strong interaction between SnF(acac)* surface species and the underlying Al_2O_3 substrate. This interaction may lead to SnF(acac)* species adsorbed to the Al_2O_3 substrate.

During the HF reaction (B), HF reacts with the underlying Al_2O_3 surface to form a new AlF_3 layer. Figure 5 illustrates that this reaction has a rapid mass change. This fast mass change is attributed to the favorable thermochemistry for the $Al_2O_3 + 6HF \rightarrow 2AlF_3 + 3H_2O$ reaction.[28] The formation of the AlF_3 layer also leads to the removal of the SnF(acac)* species. The reaction of HF with SnF(acac)* species to form SnF_2 can not be ruled out. However, SnF_2 surface species would be expected to react with $Sn(acac)_2$ to form SnF(acac)* again during the $Sn(acac)_2$ exposure. In addition, HF also provides hydrogen to form H_2O as a reaction product. This reaction removes the oxygen in Al_2O_3. The AlF_3 layer is then ready for the next $Sn(acac)_2$ reaction.

The overall proposed reaction can be expressed as

$$Al_2O_3 + 6HF + 6Sn(acac)_2 \rightarrow 2Al(acac)_3 + 6SnF(acac) + 3H_2O \quad (1)$$

This overall reaction can be divided into the $Sn(acac)_2$ and HF reactions:

$$Al_2O_3|2AlF_3* + 6Sn(acac)_2 \rightarrow Al_2O_3|xSnF(acac)* + 2Al(acac)_3 + (6 - x)SnF(acac) \quad (2)$$

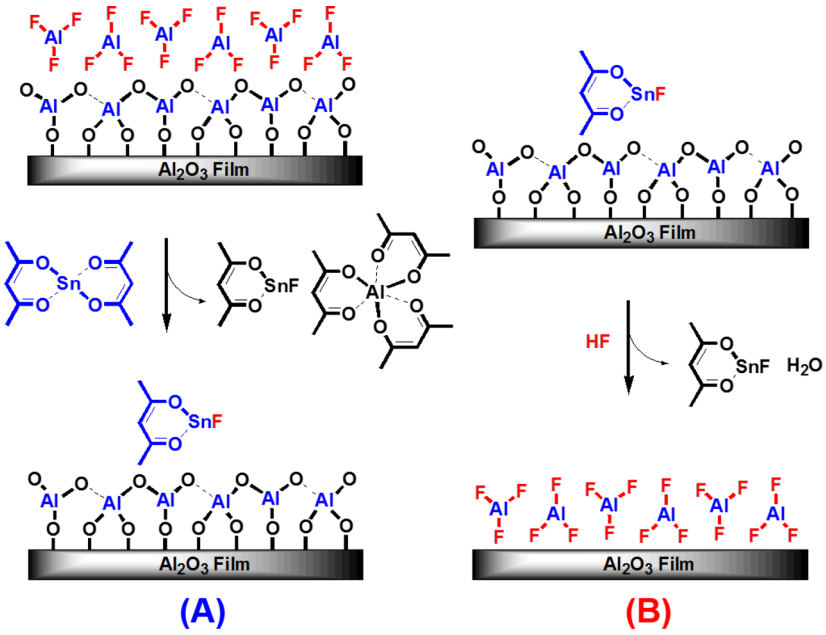

Figure 9. Schematic of proposed reaction mechanism for Al_2O_3 ALE showing (A) $Sn(acac)_2$ reaction and (B) HF reaction.

$$Al_2O_3|xSnF(acac)^* + 6HF \rightarrow 2AlF_3^* + xSnF(acac) + 3H_2O \quad (3)$$

The asterisks indicate the surface species and the vertical lines are used to separate the various surface species. The Al_2O_3 shown in eqs 2 and 3 is the amount of Al_2O_3 that is etched in one Al_2O_3 ALE cycle. x is a parameter determined by the ΔM_{Sn} and ΔM_{HF} mass changes. To obtain agreement with the ΔM_{Sn} and ΔM_{HF} mass changes in Table 1, x = 0.74, 0.46, 0.29, 0.19, and 0.15 at 150, 175, 200, 225, and 250 °C, respectively. Note that AlF_3 is the key reaction intermediate. The production of all the $Al(acac)_3$ is assumed to occur during eq 2. This assumption needs to be confirmed by mass spectrometry studies. $Al(acac)_3$ is a stable metal β-diketonate with a vapor pressure of ~3−4 Torr at 150 °C.[32−34]

The temperature dependence of ΔM_{Sn} and ΔM_{HF} is believed to be dependent on the surface species present after the $Sn(acac)_2$ and HF exposures. The larger mass gains after the $Sn(acac)_2$ exposure and the larger mass losses after the HF exposure at lower temperatures can be explained by more $Sn(acac)_2$ adsorption products on the surface after the $Sn(acac)_2$ exposure at lower temperatures. The larger mass gains after the HF exposure and the larger mass losses after the $Sn(acac)_2$ exposure at higher temperatures can be explained by more AlF_3 species on the surface after the HF exposure at higher temperatures.

Eqs 2 and 3 present the surface chemistry for the $Sn(acac)_2$ and HF reactions as determined by the QCM measurements. Complementary *in situ* Fourier transform infrared (FTIR) vibrational spectroscopy studies have shown that there are surface species that do not change during the $Sn(acac)_2$ and HF reactions. These surface species are not observed by the QCM measurements that only detect a change in mass. More detail on the reaction mechanism and the temperature dependence of Al_2O_3 ALE using both QCM and FTIR studies will be presented in another publication.[29]

Generality and Advantages of Thermal ALE Approach. The ALE of other materials including metal oxides, metal nitrides, metal phosphides, metal sulfides and metal arsenides should be possible using sequential, self-limiting thermal reactions with $Sn(acac)_2$ and HF as the reactants. $Sn(acac)_2$ can readily react with fluorine to form SnF(acac). Sn−F bond formation is expected to be favorable because tin has a high affinity for fluorine.[35] The Sn−F bond enthalpy is 466.5 kJ/mol in the diatomic SnF molecule.[36] The reaction of $Sn(acac)_2$ with fluorine to form SnF(acac) enables $Sn(acac)_2$ to release an acac ligand to the surface. Metals easily form complexes with acac ligands and have comparable stabilities.[37] The hydrogen from HF can combine with either oxygen, nitrogen, phosphorus, sulfur or arsenic from the metal oxide, metal nitride, metal phosphide, metal sulfide or metal arsenide to form H_2O, NH_3, PH_3, H_2S or AsH_3, respectively.

ALE reactions for various metal oxides, metal nitrides, metal phosphides, metal sulfides, and metal arsenides are given in Table 2. The ALE of many other metal oxides, metal nitrides, metal phosphides, metal sulfides and metal arsenides may also be possible using $Sn(acac)_2$ and HF. The reaction efficiency may be dependent on the volatility of the metal acetylacetonate reaction product. For example, many metal oxides, in addition to Al_2O_3, should be etched by the $Sn(acac)_2$ and HF reactants including HfO_2, ZrO_2, Fe_2O_3, Co_2O_3, Cr_2O_3, Sc_2O_3 and Ga_2O_3.

TABLE 2. Atomic Layer Etching Reactions for Various Materials

Metal Oxides

$Al_2O_3 + 6Sn(acac)_2 + 6HF \rightarrow 2Al(acac)_3 + 6SnF(acac) + 3H_2O$

$HfO_2 + 4Sn(acac)_2 + 4HF \rightarrow Hf(acac)_4 + 4SnF(acac) + 2H_2O$

Metal Nitrides

$GaN + 3Sn(acac)_2 + 3HF \rightarrow Ga(acac)_3 + 3SnF(acac) + NH_3$

$InN + 3Sn(acac)_2 + 3HF \rightarrow In(acac)_3 + 3SnF(acac) + NH_3$

Metal Phosphides

$AlP + 3Sn(acac)_2 + 3HF \rightarrow Al(acac)_3 + 3SnF(acac) + PH_3$

$InP + 3Sn(acac)_2 + 3HF \rightarrow In(acac)_3 + 3SnF(acac) + PH_3$

Metal Sulfides

$ZnS + 2Sn(acac)_2 + 2HF \rightarrow Zn(acac)_2 + 2SnF(acac) + H_2S$

$PbS + 2Sn(acac)_2 + 2HF \rightarrow Pb(acac)_2 + 2SnF(acac) + H_2S$

Metal Arsenides

$GaAs + 3Sn(acac)_2 + 3HF \rightarrow Ga(acac)_3 + 3SnF(acac) + AsH_3$

$InAs + 3Sn(acac)_2 + 3HF \rightarrow In(acac)_3 + 3SnF(acac) + AsH_3$

These metal oxides all produce etch products, $M(acac)_3$ or $M(acac)_4$, with vapor pressures of ~1 Torr at 150 °C.[34,38,39]

The ALE of elemental metals could also be performed using sequential exposures of $Sn(acac)_2$ and HF. The surface of the elemental metal would first be oxidized using an oxidant such as O_2 or O_3. The metal oxide could then be etched with $Sn(acac)_2$ and HF. Alternatively, the surface of the elemental metal could be nitrided, phosphided, sulfided or arsenided prior to etching the metal nitride, metal phosphide, metal sulfide or metal arsenide, respectively, with $Sn(acac)_2$ and HF.

Other Sn β-diketonates may also serve as etching reactants besides $Sn(acac)_2$ with acac = acetylacetonate. Many other β-diketone ligands on the Sn metal center are possible such as hfac = hexafluoroacetylacetonate, tfac = trifluoroacetylacetonate, and tmhd = tetramethylheptanedionate.[35,40] Different β-diketone ligands can change the physical properties of the metal β-diketonate.[37] For example, fluorine substituted β-diketone ligands generally show higher vapor pressure.[37]

Other metal β-diketonates, in addition to Sn-based compounds, could also react with HF to yield β-diketone ligands that could then form the etch products. The possible advantage of using different metal β-diketonates may be their more favorable vapor pressure, thermal stability, reaction kinetics or thermochemistry. Metal β-diketonates with metals in higher oxidation states can bind to more β-diketone ligands.[33,34] The larger number of β-diketone ligands may facilitate the etching of the metal oxide. However, $Sn(acac)_2$ with tin in the +2 oxidation state has an open coordination sphere and a readily available electron lone-pair that may facilitate fluorine binding to tin.[35]

There is also the possibility that the ALE of metal oxides would be possible with HCl or HBr instead of HF as a reactant. For example, the reaction of HCl with $Sn(acac)_2$ could produce SnCl(acac). This Sn chloride β-diketonate compound was produced earlier by the reaction of $Sn(acac)_2$ and $SnCl_2$.[35,40] The Sn−Cl bond energy in the diatomic SnCl molecule is 414 kJ/mol.[41] This bond energy is only slightly less than the bond energy of 466.5 kJ/mol in the diatomic SnF molecule.[36,41]

The advantage of using HCl or HBr would be avoiding the use of HF and its safety concerns. However, HCl and HBr are also chemically corrosive. A possible disadvantage of HCl or HBr is the lower stability of metal chlorides and metal bromides compared with metal fluorides for metal oxides, metal nitrides, metal phosphides and metal arsenides. The AlF_3 layer plays a key role as a reaction intermediate in the proposed reaction mechanism for Al_2O_3 ALE. The stability of the metal fluoride reaction intermediate may be critical for the ALE mechanism for self-limiting reactions based on $Sn(acac)_2$ and HF.

The absolute etch rate may also differ between various metal oxides during ALE with $Sn(acac)_2$ and HF as the reactants. The etch rate may be dependent upon the residual coverage of acetylacetonate species on the metal oxide surface. Higher acetylacetonate coverages may block surface sites and prevent the adsorption of $Sn(acac)_2$ or formation of the metal fluoride layer. This site-blocking by acetylacetonate surface species may reduce the etch rate. Site-blocking by hfac and hfacH was recently demonstrated during Pt ALD and Pd ALD using $Pt(hfac)_2$ and $Pd(hfac)_2$, respectively.[30,31] The temperature dependence of the Al_2O_3 ALE may be attributed to the lower residual coverage of acetylacetonate surface species at higher temperatures. Other ligands on the metal β-diketonate may alter the residual coverage of ligands on the metal oxide surface and change the etch rate.

There are advantages to the thermal ALE approach compared with ALE based on halogen adsorption and ion or energetic neutral noble atom bombardment. The thermal ALE approach avoids any damage to the underlying substrate resulting from high energy ions or energetic neutrals. Ions from plasmas have been implicated in the performance degradation of high-k/metal gate stacks.[42] Using neutral noble gas beams is able to mitigate the structural and electrical damage caused by ions.[8]

ALE based on ion or neutral noble atom bombardment also requires line-of-sight to the substrate. This requirement can be used advantageously to minimize undercutting with directional ions or energetic neutral atoms during ALE. However, this line-of-sight requirement is detrimental if conformality is required for the etching. The line-of-sight requirement is also limited to the relatively small surface areas that are subjected to ion or neutral noble atom bombardment. The thermal ALE approach will be particularly important for etching high surface area and high aspect ratio structures.

CONCLUSIONS

Al_2O_3 ALE was observed using $Sn(acac)_2$ and HF as the reactants. The sequential, self-limiting thermal reactions of $Sn(acac)_2$ and HF etched Al_2O_3 linearly with atomic level precision. Al_2O_3 ALE was demonstrated at temperatures from 150 to 250 °C. The sequential $Sn(acac)_2$ and HF reactions were self-limiting *versus* reactant exposure as revealed by QCM studies. The QCM studies also measured MCPC values that increased with temperature from −4.1 ng/(cm^2 cycle) at 150 °C to −18.3 ng/(cm^2 cycle) at 250 °C. These MCPC values correspond to etch rates from 0.14 Å/cycle at 150 °C to 0.61 Å/cycle at 250 °C. The linear removal of Al_2O_3 was confirmed by XRR analysis. The XRR studies measured Al_2O_3 ALE etch rates of 0.27 Å/cycle at 200 °C. The Al_2O_3 films also remained smooth during Al_2O_3 ALE.

The overall etching reaction is believed to follow the reaction $Al_2O_3 + 6Sn(acac)_2 + 6HF \rightarrow 2Al(acac)_3 + 6SnF(acac) + 3H_2O$. In the proposed reaction mechanism, AlF_3 is the key reaction intermediate. The $Sn(acac)_2$ reactant donates acac to the AlF_3 layer on the Al_2O_3 substrate to produce $Al(acac)_3$. The HF reactant forms the AlF_3 reaction intermediate from Al_2O_3 and allows SnF(acac) and H_2O to leave as reaction products. The ALE of many other metal oxides besides Al_2O_3 should also be possible using $Sn(acac)_2$, or other metal β-diketonates, together with HF. This ALE reaction mechanism should also be applicable for the ALE of metal nitrides, metal phosphides, metal sulfides and metal arsenides.

METHODS

Viscous Flow Reactor Equipped for *In Situ* QCM Measurements. The ALE reactions at 150−250 °C were performed in a viscous flow ALD reactor.[43,44] A proportional-integral-derivative (PID) temperature controller (2604, Eurotherm) stabilized the temperature in the reactor to within ±0.04 °C. A capacitance manometer (Baratron 121A, MKS) measured the pressure in the reactor. The ALD reactor was equipped with an *in situ* quartz crystal microbalance (QCM).[43] The RC-cut quartz crystal[45] (gold coated and polished, 6 MHz, Colnatec) was placed in a sensor head (BSH-150, Inficon) and then sealed with high temperature epoxy (Epo-Tek H21D, Epoxy technology). All *in situ* QCM measurements were recorded by a thin film deposition monitor (Maxtek TM-400, Inficon).

The Al_2O_3 ALE reactions were performed using sequential exposure of tin(II) acetylacetonate ($Sn(acac)_2$, 37−38% Sn, Gelest) and HF-pyridine (70 wt % HF, Sigma-Aldrich). HF-pyridine is a liquid at room temperature and has an equilibrium with gaseous HF.[46] The HF pressure from HF-pyridine is >2−3 Torr at room temperature. The two pneumatic valves and one metering valve used for HF dosing produced HF pressure transients of ~80 mTorr. HF-pyridine enabled the safe handling of anhydrous HF. Note that HF-pyridine can be dangerous if not utilized properly. $Sn(acac)_2$ and HF-pyridine were transferred to stainless steel bubblers in a dry N_2-filled glovebag. The stainless steel bubbler containing $Sn(acac)_2$ was held at 100 °C. The one pneumatic valve used for $Sn(acac)_2$ dosing produced $Sn(acac)_2$ pressure transients of ~20 mTorr. The Al_2O_3 films were grown with Al_2O_3 ALD using TMA (97%, Sigma-Aldrich) and H_2O (Chromasolv for HPLC, Sigma-Aldrich). The HF-pyridine, TMA, and H_2O precursors were maintained at room temperature.

The reactor was pumped using a mechanical pump (Pascal 2015SD, Alcatel). The base pressure of the reactor without any N_2 flow was ~10 mTorr. Separate mass flow controllers were used to provide N_2 carrier gas for each reactant. An additional mass flow controller streamed N_2 gas through the reactor. These three separate mass flow controllers (Type 1179A, MKS) delivered a constant total flow of 150 sccm of ultra high purity (UHP) N_2 carrier gas into the reactor. Additional N_2 gas flow of 20 sccm using a metering bellows-sealed valve (SS-4BMG, Swagelok) prevented deposition on the backside of the QCM crystal.[43] The total N_2 gas flow of 170 sccm produced a background N_2 pressure of ~1 Torr in the reactor.

Sample Preparation and *Ex Situ* Film Analysis. Boron-doped Si(100) wafers (p-type, Silicon Valley Microelectronics) were cut into samples with dimensions of 2.5 cm by 2.5 cm. These substrates were used for Al_2O_3 ALD deposition. The Si wafers were first rinsed with acetone, isopropanol, and deionized water. Subsequently, the Si wafers were dried with UHP N_2 gas.

The *ex situ* X-ray reflectivity (XRR) scans were recorded by a high resolution X-ray diffractometer (Bede D1, Jordan Valley Semiconductors) using Cu Kα (λ = 1.540 Å) radiation. The filament voltage and current in the X-ray tube were 40 kV and 35 mA, respectively. A 10 arcsec step size and a 5 s acquisition time were used for recording all XRR scans with a range of 300 to 6000 arcsec. The analysis software (Bede REFS, Jordan Valley Semiconductors) fitted the XRR scans to determine film thickness, film density and surface roughness.

Spectroscopic ellipsometry (SE) determined the film thicknesses and refractive index. The measurement of Ψ and Δ were recorded using a spectroscopic ellipsometer (M-2000, J. A. Woollam) with a spectral range of 240 to 1700 nm and an incidence angle of 75°. The analysis software (CompleteEASE, J. A. Woollam) fitted Ψ and Δ based on a Sellmeier model to determine the thicknesses and refractive index of the film.[47]

X-ray photoemission spectroscopy (XPS) analysis was performed using a PHI 5600 X-ray photoelectron spectrometer using a monochromatic Al Kα source. The XPS data were collected using Auger Scan (RBD Instruments). The XPS data were analyzed in CASA XPS (Casa Software Ltd.). Atomic force microscope (AFM) analysis was performed using an EasyScan 2 (Nanosurf) with a dynamic force module. The scan software (EasyScan 2, Nanosurf) measured the RMS roughness using a 5 μm × 5 μm image size.

Conflict of Interest: The authors declare no competing financial interest.

Acknowledgment. This research was funded by the National Science Foundation (CHE-1306131). Additional personnel support for Y.L. was provided by the Department of Energy through the DOE-BATT program. The authors thank Huaxing Sun for the X-ray photoelectron spectroscopy (XPS) analysis of elemental film composition. The authors also thank Timothy J. Porcelli for the atomic force microscopy (AFM) measurements of surface roughness.

REFERENCES AND NOTES

1. George, S. M. Atomic Layer Deposition: An Overview. *Chem. Rev.* **2010**, *110*, 111–131.
2. Miikkulainen, V.; Leskela, M.; Ritala, M.; Puurunen, R. L. Crystallinity of Inorganic Films Grown by Atomic Layer Deposition: Overview and General Trends. *J. Appl. Phys.* **2013**, *113*, 021301.
3. Profijt, H. B.; Potts, S. E.; van de Sanden, M. C. M.; Kessels, W. M. M. Plasma-Assisted Atomic Layer Deposition: Basics, Opportunities, and Challenges. *J. Vac. Sci. Technol., A* **2011**, *29*, 050801.

4. Agarwal, A.; Kushner, M. J. Plasma Atomic Layer Etching Using Conventional Plasma Equipment. *J. Vac. Sci. Technol., A* **2009**, *27*, 37–50.
5. Athavale, S. D.; Economou, D. J. Molecular Dynamics Simulation of Atomic Layer Etching of Silicon. *J. Vac. Sci. Technol., A* **1995**, *13*, 966–971.
6. Athavale, S. D.; Economou, D. J. Realization of Atomic Layer Etching of Silicon. *J. Vac. Sci. Technol., B* **1996**, *14*, 3702–3705.
7. Kubota, N. A.; Economou, D. J.; Plimpton, S. J. Molecular Dynamics Simulations of Low-Energy (25−200 eV) Argon Ion Interactions with Silicon Surfaces: Sputter Yields and Product Formation Pathways. *J. Appl. Phys.* **1998**, *83*, 4055–4063.
8. Park, S. D.; Lim, W. S.; Park, B. J.; Lee, H. C.; Bae, J. W.; Yeom, G. Y. Precise Depth Control and Low-Damage Atomic-Layer Etching of HfO_2 using BCl_3 and Ar Neutral Beam. *Electrochem. Solid State Lett.* **2008**, *11*, H71–H73.
9. Sakaue, H.; Iseda, S.; Asami, K.; Yamamoto, J.; Hirose, M.; Horiike, Y. Atomic Layer Controlled Digital Etching of Silicon. *Jpn. J. Appl. Phys. 1* **1990**, *29*, 2648–2652.
10. Yamamoto, J.; Kawasaki, T.; Sakaue, H.; Shingubara, S.; Horiike, Y. Digital Etching Study and Fabrication of Fine Si Lines and Dots. *Thin Solid Films* **1993**, *225*, 124–129.
11. Matsuura, T.; Sugiyama, T.; Murota, J. Atomic-Layer Surface Reaction of Chlorine on Si and Ge Assisted by an Ultraclean ECR Plasma. *Surf. Sci.* **1998**, *402*, 202–205.
12. Sugiyama, T.; Matsuura, T.; Murota, J. Atomic-Layer Etching of Ge Using an Ultraclean ECR Plasma. *Appl. Surf. Sci.* **1997**, *112*, 187–190.
13. Park, S. D.; Lee, D. H.; Yeom, G. Y. Atomic Layer Etching of Si(100) and Si(111) Using Cl_2 and Ar Neutral Beam. *Electrochem. Solid State Lett.* **2005**, *8*, C106–C109.
14. Lim, W. S.; Park, S. D.; Park, B. J.; Yeom, G. Y. Atomic Layer Etching of (100)/(111) GaAs with Chlorine and Low Angle Forward Reflected Ne Neutral Beam. *Surf. Coat. Technol.* **2008**, *202*, 5701–5704.
15. Meguro, T.; Hamagaki, M.; Modaressi, S.; Hara, T.; Aoyagi, Y.; Ishii, M.; Yamamoto, Y. Digital Etching of GaAs—New Approach of Dry Etching to Atomic Ordered Processing. *Appl. Phys. Lett.* **1990**, *56*, 1552–1554.
16. Meguro, T.; Ishii, M.; Sugano, T.; Gamo, K.; Aoyagi, Y. Control of the Etching Reaction of Digital Etching Using Tunable UV Laser Irradiation. *Appl. Surf. Sci.* **1994**, *82−3*, 193–199.
17. Maki, P. A.; Ehrlich, D. J. Laser Bilayer Etching of GaAs Surfaces. *Appl. Phys. Lett.* **1989**, *55*, 91–94.
18. Park, S. D.; Oh, C. K.; Bae, J. W.; Yeom, G. Y.; Kim, T. W.; Song, J. I.; Jang, J. H. Atomic Layer Etching of InP Using a Low Angle Forward Reflected Ne Neutral Beam. *Appl. Phys. Lett.* **2006**, *89*, 043109.
19. Min, K. S.; Kang, S. H.; Kim, J. K.; Jhon, Y. I.; Jhon, M. S.; Yeom, G. Y. Atomic Layer Etching of Al_2O_3 Using BCl_3/Ar for the Interface Passivation Layer of III-V MOS Devices. *Microelectron. Eng.* **2013**, *110*, 457–460.
20. Park, J. B.; Lim, W. S.; Park, B. J.; Park, I. H.; Kim, Y. W.; Yeom, G. Y. Atomic Layer Etching of Ultra-Thin HfO_2 Film for Gate Oxide in MOSFET Devices. *J. Phys. D: Appl. Phys.* **2009**, *42*, 055202.
21. Lim, W. S.; Park, J. B.; Park, J. Y.; Park, B. J.; Yeom, G. Y. Low Damage Atomic Layer Etching of ZrO_2 by Using BCl_3 Gas and Ar Neutral Beam. *J. Nanosci. Nanotechnol.* **2009**, *9*, 7379–7382.
22. Park, J. B.; Lim, W. S.; Park, S. D.; Park, Y. J.; Yeom, G. Y. Etch Characteristics of TiO_2 Etched by Using an Atomic Layer Etching Technique with BCl_3 Gas and an Ar Neutral Beam. *J. Korean Phys. Soc.* **2009**, *54*, 976–980.
23. Metzler, D.; Bruce, R. L.; Engelmann, S.; Joseph, E. A.; Oehrlein, G. S. Fluorocarbon Assisted Atomic Layer Etching of SiO_2 using Cyclic Ar/C_4F_8 Plasma. *J. Vac. Sci. Technol., A* **2014**, *32*, 020603.
24. Rauf, S.; Sparks, T.; Ventzek, P. L. G.; Smirnov, V. V.; Stengach, A. V.; Gaynullin, K. G.; Pavlovsky, V. A. A Molecular Dynamics Investigation of Fluorocarbon Based Layer-by-layer Etching of Silicon and SiO_2. *J. Appl. Phys.* **2007**, *101*, 033308.
25. Kim, Y. Y.; Lim, W. S.; Park, J. B.; Yeom, G. Y. Layer by Layer Etching of the Highly Oriented Pyrolythic Graphite by Using Atomic Layer Etching. *J. Electrochem. Soc.* **2011**, *158*, D710–D714.
26. Lim, W. S.; Kim, Y. Y.; Kim, H.; Jang, S.; Kwon, N.; Park, B. J.; Ahn, J.-H.; Chung, I.; Hong, B. H.; Yeom, G. Y. Atomic Layer Etching of Graphene for Full Graphene Device Fabrication. *Carbon* **2012**, *50*, 429–435.
27. Vogli, E.; Metzler, D.; Oehrlein, G. S. Feasibility of Atomic Layer Etching of Polymer Material Based on Sequential O_2 Exposure and Ar Low-Pressure Plasma-Etching. *Appl. Phys. Lett.* **2013**, *102*, 253105.
28. *HSC Chemistry*, version 5.1; Outokumpu Research Oy: Pori, Finland.
29. Lee, Y.; DuMont, J. W.; George, S. M. Mechanism of Thermal Al_2O_3 Atomic Layer Etching Using Sequential Reactions with $Sn(acac)_2$ and HF, manuscript in preparation.
30. Anderson, V. R.; Leick, N.; Clancey, J. W.; Hurst, K. E.; Jones, K. M.; Dillon, A. C.; George, S. M. Atomic Layer Deposition of Platinum Nanoparticles on Titanium Oxide and Tungsten Oxide Using Platinum(II) Hexafluoroacetylacetonate and Formalin as the Reactants. *J. Phys. Chem. C* **2014**, *118*, 8960–8970.
31. Goldstein, D. N.; George, S. M. Surface Poisoning in the Nucleation and Growth of Palladium Atomic Layer Deposition with $Pd(hfac)_2$ and Formalin. *Thin Solid Films* **2011**, *519*, 5339–5347.
32. Berg, E. W.; Truemper, J. T. Vapor Pressure-Temperature Data for Various Metal Beta-Diketone Chelates. *Anal. Chim. Acta* **1965**, *32*, 245–252.
33. Eisentraut, K. J.; Sievers, R. E. Thermogravimetric Studies of Metal Beta-Diketonates. *J. Inorg. Nucl. Chem.* **1967**, *29*, 1931–1936.
34. Fahlman, B. D.; Barron, A. R. Substituent Effects on the Volatility of Metal Beta-Diketonates. *Adv. Mater. Opt. Electron.* **2000**, *10*, 223–232.
35. Ewings, P. F. R.; Harrison, P. G.; Fenton, D. E. Derivatives of Divalent Germanium, Tin, and Lead. 5. Bis-(Pentane-2,4-Dionato)-Tin(II),Bis(1,1,1-Trifluoropentane-2,4-Dionato)-Tin(II), and Bis(1,1,1,5,5,5-Hexafluoropentane-2,4-Dionato)-Tin(II). *J. Chem. Soc., Dalton Trans.* **1975**, 821–826.
36. Zimbov, K.; Hastie, J. W.; Margrave, J. L. Mass Spectroetric Studies at High Temperatures. 24. Thermodynamics of Vaporization of SnF_2 and PbF_2 and Dissociation Energies of SnF and PbF. *Trans. Faraday Soc.* **1968**, *64*, 861–867.
37. Mehrotra, R. C.; Bohra, R.; Gaur, D. P. *Metal Beta-Diketonates and Allied Derivatives*; Academic Press: London, 1978.
38. Morozova, N. B.; Zherikova, K. V.; Baidina, I. A.; Sysoev, S. V.; Semyannikov, P. P.; Yakovkina, L. V.; Smirnova, T. P.; Gelfond, N. V.; Igumenov, I. K.; Carta, G.; Rossetto, G. Volatile Hafnium(IV) Compounds with Beta-Diketonate and Cyclopentadienyl Derivatives. *J. Phys. Chem. Solids* **2008**, *69*, 673–679.
39. Zherikova, K. V.; Morozova, N. B.; Zelenina, L. N.; Sysoev, S. V.; Chusova, T. P.; Igumenov, I. K. Thermal Properties of Hafnium(IV) and Zirconium(IV) Beta-Diketonates. *J. Therm. Anal. Calorim.* **2008**, *92*, 729–734.
40. Bos, K. D.; Budding, H. A.; Bulten, E. J.; Noltes, J. G. Tin(II) Bis(1,3-Diketonates) and Tin(II) 1,3-Diketonate Chlorides. *Inorg. Nucl. Chem. Lett.* **1973**, *9*, 961–963.
41. *CRC Handbook of Chemistry and Physics*, 85th ed.; Lide, D. R., Ed.; CRC Press: Boca Raton, FL, 2005.
42. Hussain, M. M.; Song, S.-C.; Barnett, J.; Kang, C. Y.; Gebara, G.; Sassman, B.; Moumen, N. Plasma-Induced Damage in High-k/Metal Gate Stack Dry Etch. *IEEE Electron Device Lett.* **2006**, *27*, 972–974.
43. Elam, J. W.; Groner, M. D.; George, S. M. Viscous Flow Reactor with Quartz Crystal Microbalance for Thin Film Growth by Atomic Layer Deposition. *Rev. Sci. Instrum.* **2002**, *73*, 2981–2987.
44. Lee, Y.; Yoon, B.; Cavanagh, A. S.; George, S. M. Molecular Layer Deposition of Aluminum Alkoxide Polymer Films Using Trimethylaluminum and Glycidol. *Langmuir* **2011**, *27*, 15155–15164.

45. Riha, S. C.; Libera, J. A.; Elam, J. W.; Martinson, A. B. F. Design and Implementation of an Integral Wall-Mounted Quartz Crystal Microbalance for Atomic Layer Deposition. *Rev. Sci. Instrum.* **2012**, *83*, 094101.
46. Olah, G. A.; Nojima, M.; Kerekes, I. Synthetic Methods and Reactions 0.2. Hydrofluorination of Alkenes, Cyclopropane and Alkynes with (Trialkylamine) Reagents. *Synthesis* **1973**, *12*, 779–780.
47. Shannon, R. D.; Shannon, R. C.; Medenbach, O.; Fischer, R. X. Refractive Index and Dispersion of Fluorides and Oxides. *J. Phys. Chem. Ref. Data* **2002**, *31*, 931–970.